



Article

Analytical Prediction of Strip Foundation Building Response to Shallow Tunneling Considering the Tunneling Process

Lin Yu ^{1,2} , Dingli Zhang ¹, Qian Fang ^{1,*}, Yujie Li ², Gang Wang ² and Liqiang Cao ³ 

¹ Key Laboratory of Urban Underground Engineering of Ministry of Education, Beijing Jiaotong University, Beijing 100044, China; 16115284@bjtu.edu.cn (L.Y.); dlzhang@bjtu.edu.cn (D.Z.)

² Beijing Mass Transit Railway Operation Corp., Ltd., Beijing 100044, China; 15901112566@163.com (Y.L.); 13910119588@163.com (G.W.)

³ College of Civil and Transportation Engineering, Shenzhen University, Shenzhen 518060, China; liqiangcao@bjtu.edu.cn

* Correspondence: qfang@bjtu.edu.cn; Tel.: +86-10-51688115

Abstract: This paper presents an analytical method to predict the response of a strip foundation building to shallow tunneling based on the two-stage method. The existing building is simplified as a Euler–Bernoulli beam resting on the Pasternak model. The tunneling process and different relative positions between the tunnel and the existing building can be considered in the proposed method. The accuracy of the proposed method is verified through comparisons with results from the finite element and finite difference methods. The results indicate that the differential settlement of the building reaches a maximum and the rotation angles are symmetric with respect to the building centerline when the tunnel face arrives at the middle of the building. The maximum bending moments occur at the middle of the building, while the maximum shear forces occur at about one-fifth and four-fifths of the building length when the tunnel face is located at the two ends of the building. According to the parametric analysis, the alignment angle, elastic modulus and Poisson’s ratio of the soil, bending stiffness, and gap parameter greatly affect the building response.

Keywords: building response; soil–building interaction; ground settlement; tunneling process; Pasternak model



Citation: Yu, L.; Zhang, D.; Fang, Q.; Li, Y.; Wang, G.; Cao, L. Analytical Prediction of Strip Foundation Building Response to Shallow Tunneling Considering the Tunneling Process. *Appl. Sci.* **2022**, *12*, 4656. <https://doi.org/10.3390/app12094656>

Academic Editor: Edyta Plebankiewicz

Received: 13 April 2022

Accepted: 4 May 2022

Published: 6 May 2022

Publisher’s Note: MDPI stays neutral with regard to jurisdictional claims in published maps and institutional affiliations.



Copyright: © 2022 by the authors. Licensee MDPI, Basel, Switzerland. This article is an open access article distributed under the terms and conditions of the Creative Commons Attribution (CC BY) license (<https://creativecommons.org/licenses/by/4.0/>).

1. Introduction

In densely built urban areas, there is an increasing demand for further development of underground transit systems due to the lack of surface space, which promotes the excavation of shallowly buried tunnel crossing beneath existing buildings. Shallow tunneling in soft ground inevitably entails the generation of stress relief and ground settlement around the tunnel [1–3]. The critical factors affecting ground settlement around the tunnel are essentially the physical and mechanical parameters of the soil and tunnel. The excessive ground settlement eventually transfers to the building foundation, and is responsible for the potential deformation or even damage of the existing buildings [4–6]. To ensure the safety and serviceability of the existing buildings, reliable assessment of the influences of shallow tunneling on the existing buildings is necessary for engineers, and is always a serious concern.

Considerable efforts have been made to investigate the response of strip foundation buildings to tunnel excavation. The methods used for analyzing this problem can be broadly classified as theoretical analysis, numerical simulation, model testing, and field monitoring. In theoretical analysis, researchers developed a two-stage method to rapidly predict the building deformation [7–11] or damage [12–15] induced by shallow tunneling. The existing building is commonly considered as an equivalent elastic thick beam, Euler–Bernoulli beam, or Timoshenko beam. The ground is usually presented by the Winkler model or the Pasternak model. Numerical simulation provides insights into the building

response with different characteristics subjected to the tunneling-induced ground settlement. Refined numerical models were established using the finite element method [16–20], finite difference method [21], and discrete element method [22], while the tunnel, soil, and building are computed as a whole. Model testing is capable of creating similar conditions in a small-scale model to those of the full-scale prototype. The centrifuge model tests [23–25] and the 1 g model tests [26–28] can both serve as effective tools to study the interaction between the shallow buried tunnel and the existing building. Field monitoring is the most straightforward method for analyzing the displacements and cracks of the building strip foundation that result from tunneling, and has been widely employed by researchers in practice [29–33].

Current studies using theoretical analysis mainly focus on the case of the building axis perpendicular to the tunnel axis under plane strain condition without considering the effects of the tunneling process. To gain a better mechanical understanding of the strip foundation building response arising from tunnel excavation, a new analytical method taking into account the tunneling process is proposed in this paper. The proposed method can be applied to the condition that the angle between the building axis and the tunnel axis is arbitrary. The building response obtained from the proposed method is verified by comparing with results from the finite element and finite difference methods. Based on the verified analytical solutions, a parametric analysis is performed to systematically explore the effects of different factors on the building deformation and internal forces.

2. Method of Analysis

The two-stage method based on the Pasternak model [34] is adopted in this study to investigate the tunnel–soil–building interaction. Therefore, the analysis comprises two stages: (1) estimation of the greenfield ground settlement due to shallow tunneling and (2) calculation of the building response to these greenfield ground settlements. Note that the hypothesis of this method is that the tunneling-induced ground settlement is not affected by the presence of the existing building.

2.1. Three-Dimensional Greenfield Ground Settlements

The sign convention utilized for estimating the greenfield ground settlement induced by tunnel excavation is shown in Figure 1. Considering the nonuniform convergence and the ovalization, Yu [35] modified the plane strain solutions presented by Loganathan and Poulos [36] and derived the three-dimensional solutions, which are suitable for clayey and sandy soils and can be written as follows:

$$w_1 = \eta \varepsilon_m R^2 \left\{ \frac{H-z_1}{x_1^2 + (H-z_1)^2} + \frac{(3-4\nu)(H+z_1)}{x_1^2 + (H+z_1)^2} - \frac{2z_1[x_1^2 - (H+z_1)^2]}{[x_1^2 + (H+z_1)^2]^2} \right\} + \eta \delta R^2 \left(\frac{(H+z_1)[k_1 x_1^2 - (H+z_1)^2]}{[x_1^2 + (H+z_1)^2]^2} - \frac{(H-z_1)[k_1 x_1^2 - (H-z_1)^2]}{[x_1^2 + (H-z_1)^2]^2} - 2H \left\{ \frac{x_1^2 - (H+z_1)^2}{[x_1^2 + (H+z_1)^2]^2} + \frac{m}{m+1} \frac{2z_1(H+z_1)[3x_1^2 - (H+z_1)^2]}{[x_1^2 + (H+z_1)^2]^3} \right\} \right) \quad (1)$$

with

$$\varepsilon_m = \frac{4Rg + g^2}{4R^2} \exp \left\{ -\frac{1.38x_1^2}{[H/\tan(45^\circ + \varphi/2) + R]^2} - \frac{0.69z_1^2}{H^2} \right\} \quad (2)$$

$$\delta = \frac{4Rg + g^2}{40R^2} \quad (3)$$

$$\eta = \frac{1}{2} \left[1 - \frac{y_1 - d}{\sqrt{x_1^2 + (y_1 - d)^2 + H^2}} \right] \quad (4)$$

where ε_m and δ are the modified equivalent ground-loss parameter and the ovalization parameter, respectively; g is the gap parameter evaluated by Lee et al. [37]; η represents the spatial deformation factor; R and H are the tunnel radius and the depth to the tunnel axis, respectively; $m = 1/(1 - 2\nu)$; $k_1 = \nu/(1 - \nu)$; φ and ν denote the internal friction angle and the Poisson's ratio of the soil, respectively; and d is the distance between the point with 50% of the maximum surface settlement $w_{1,max}$ and the tunnel face (Figure 1). The value of d can be reasonably considered as $-3.0D - D$ [38], and D is the tunnel diameter.

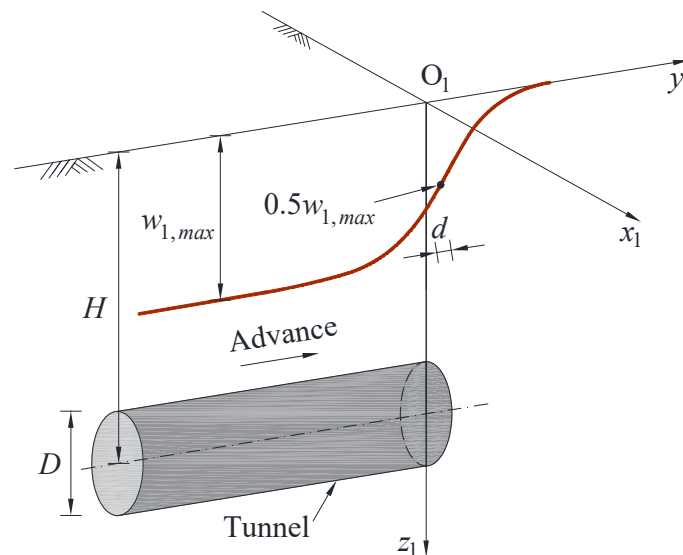


Figure 1. Greenfield surface settlement above a tunnel axis.

2.2. Solutions of Building Response

The relative position between the shallowly buried tunnel and the strip foundation building in the general case is shown in Figure 2. Two coordinate systems are established to facilitate analysis (Figure 3). The origin O_1 and O are set at the tunnel face and the left end of the building (the end of the building that is first passed by the tunnel face), respectively. The coordinates of the ground and the existing building are described as (x_1, y_1, z_1) and (x, y, z) , respectively. A unit width B is taken along the short side of the existing building [13]. The building axis (parallel to the long side of the existing building) is aligned with x_1 -axis at an angle α , and $\alpha > 0$ indicates the counterclockwise alignment. The relationship between the two coordinate systems can be obtained as follows:

$$\begin{cases} x_1 = (y + s_2) \cos \alpha \\ y_1 = (y + s_2) \sin \alpha + s_1 \\ z_1 = z \end{cases} \quad (5)$$

where s_1 is the distance between the origin O_1 and the intersection of the building axis and the y_1 -axis; s_2 is the distance between the origin O and the intersection of the building axis and the y_1 -axis.

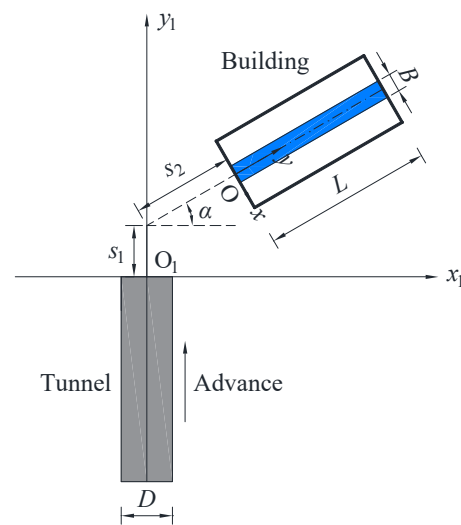


Figure 2. Plan view of tunnel and building.

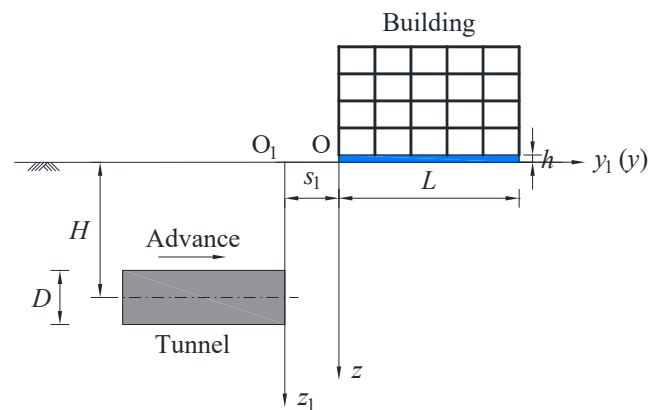


Figure 3. Profile view of building axis parallel to tunnel axis.

In the second stage, the existing building is simplified as an Euler–Bernoulli beam with the equivalent stiffness on the Pasternak model, as shown in Figure 4, which is able to consider the interaction between adjacent springs. The masonry building and the framed building with strip foundations are simplified as the pure bending beam and the shear bending beam in this work, respectively [39]. It is assumed that the building foundation is always in contact with the underlying soil, and there is no slippage on the soil–foundation interface. Additionally, the soil is assumed to be isotropic elastic material and the plastic behavior of the soil is not involved here. Then, the subgrade reaction can be expressed as

$$p(y) = k[w(y) - w_1(x_1, y_1)] - G_p \frac{d^2[w(y) - w_1(x_1, y_1)]}{dy^2} \quad (6)$$

where $w(y)$ is the building settlement; $w_1(x_1, y_1)$ is the greenfield surface settlement at the corresponding building location calculated by Equation (1); k and G_p denote the coefficient of the subgrade modulus [40] and the shear stiffness of the subgrade [41], respectively, which are given by

$$k = \frac{0.65E_s}{B(1-\nu^2)} \sqrt[12]{\frac{E_s B^4}{EI}} \quad (7)$$

$$G_p = \frac{E_s t}{6(1+\nu)} \quad (8)$$

where E_s is the elastic modulus of the soil; EI is the equivalent bending stiffness of the existing building; and t is the thickness of the elastic layer, with $t = 2.5B$, as suggested by

Xu [42]. Note that when G_p is equal to zero, the Pasternak model can be degenerated into the Winkler model.

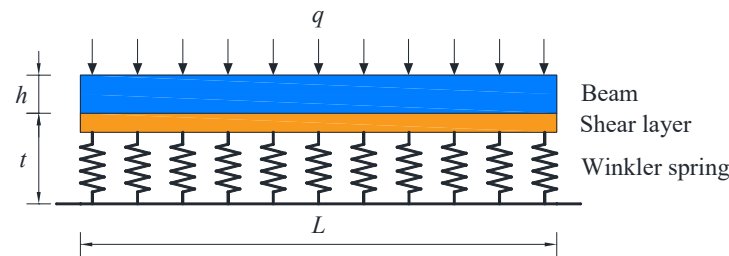


Figure 4. Soil–building interaction model.

By imposing the greenfield surface settlement on the existing building, the governing differential equation for the building settlement is provided below [43]:

$$EI \frac{d^4 w(y)}{dy^4} - G \frac{d^2 w(y)}{dy^2} + kBw(y) = Bf(x_1, y_1) \quad (9)$$

where G represents the shear stiffness parameter, with $G = G_p B$ for masonry buildings and $G = G_f + G_{c1} + G_p B$ for framed buildings; G_f is the equivalent shear stiffness of the framed building; G_{c1} is the linear bending stiffness of the columns on the bottom story. The values of G_f and G_{c1} can be determined with reference to Xia et al. [44]; $f(x_1, y_1)$ denotes the additional load on the existing building and can be expressed as

$$f(x_1, y_1) = q + kw_1(x_1, y_1) - G_p \frac{d^2 w_1(x_1, y_1)}{dy^2} \quad (10)$$

where q is the equivalent vertical uniform pressure of the building acting on the subgrade.

Since it is difficult to obtain an analytical solution of Equation (10), the finite difference method is used herein to solve Equation (10) numerically. As shown in Figure 5, the beam is divided into n elements of length $l = L/n$, and L is the beam length. For the purpose of the differential operation, extra two virtual nodes are added at the two ends of the beam. Regarding the particular node i , the following central difference forms can be deduced:

$$\left(\frac{dw}{dy} \right)_i = \frac{-(w_{i+2} - w_{i-2}) + 8(w_{i+1} - w_{i-1})}{12l} \quad (11)$$

$$\left(\frac{d^2 w}{dy^2} \right)_i = \frac{-(w_{i+2} + w_{i-2}) + 16(w_{i+1} + w_{i-1}) - 30w_i}{12l^2} \quad (12)$$

$$\left(\frac{d^3 w}{dy^3} \right)_i = \frac{(w_{i+2} - w_{i-2}) - 2(w_{i+1} - w_{i-1})}{2l^3} \quad (13)$$

$$\left(\frac{d^4 w}{dy^4} \right)_i = \frac{(w_{i+2} + w_{i-2}) - 4(w_{i+1} + w_{i-1}) + 6w_i}{l^4} \quad (14)$$

where w_{i-2} , w_{i-1} , w_i , w_{i+1} , and w_{i+2} are the beam settlements at the nodes $i - 2$, $i - 1$, i , $i + 1$, and $i + 2$, respectively.

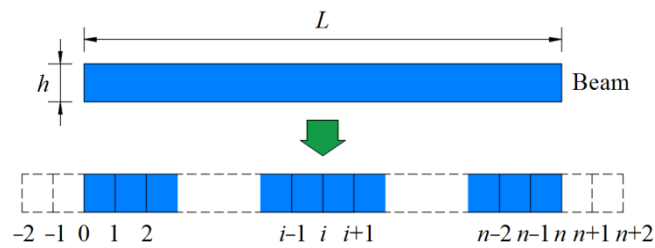


Figure 5. Discretization of beam.

Substituting Equations (12) and (14) into Equation (9), the fourth-order nonhomogeneous differential equation can be converted into the finite difference form:

$$a_1 w_{i-2} + a_2 w_{i-1} + a_3 w_i + a_2 w_{i+1} + a_1 w_{i+2} = f_i(x_1, y_1) \quad (15)$$

with

$$\begin{bmatrix} a_1 \\ a_2 \\ a_3 \end{bmatrix} = \begin{bmatrix} 1 & \frac{1}{12} & 0 \\ -4 & -\frac{4}{3} & 0 \\ 6 & \frac{5}{2} & 1 \end{bmatrix} \begin{bmatrix} \frac{EI}{Bl^4} \\ \frac{G}{Bl^2} \\ k \end{bmatrix} \quad (16)$$

According to the Euler–Bernoulli beam theory, the rotation angle θ_i , bending moment M_i , and shear force Q_i of the beam at the node i can be expressed as follows:

$$\theta_i = \left(\frac{dw}{dy} \right)_i = \frac{1}{12l} (w_{i-2} - 8w_{i-1} + 8w_{i+1} - w_{i+2}) \quad (17)$$

$$M_i = -EI \left(\frac{d^2 w}{dy^2} \right)_i = -\frac{EI}{12l^2} (-w_{i-2} + 16w_{i-1} - 30w_i + 16w_{i+1} - w_{i+2}) \quad (18)$$

$$Q_i = -EI \left(\frac{d^3 w}{dy^3} \right)_i = -\frac{EI}{2l^3} (-w_{i-2} + 2w_{i-1} - 2w_{i+1} + w_{i+2}) \quad (19)$$

The two ends of the beam are supposed to satisfy the free boundary condition. Consequently, both the bending moments and the shear forces at the nodes 0 and n are not produced. These boundary conditions can be described as

$$M_0 = M_n = 0 \quad (20)$$

$$Q_0 = Q_n = 0 \quad (21)$$

Combining Equations (18)–(21), the settlements for the four virtual nodes -2 , -1 , $n+1$, and $n+2$ can be obtained:

$$w_{-2} = \frac{30}{7} w_0 - \frac{32}{7} w_1 + \frac{9}{7} w_2 \quad (22)$$

$$w_{-1} = \frac{15}{7} w_0 - \frac{9}{7} w_1 + \frac{1}{7} w_2 \quad (23)$$

$$w_{n+1} = \frac{15}{7} w_n - \frac{9}{7} w_{n-1} + \frac{1}{7} w_{n-2} \quad (24)$$

$$w_{n+2} = \frac{30}{7} w_n - \frac{32}{7} w_{n-1} + \frac{9}{7} w_{n-2} \quad (25)$$

By assembling the finite difference equations for each node, the settlement–load relationship of the beam Equation (15) can be rewritten in the matrix form as

$$\{W\} = [K]^{-1} \{F\} \quad (26)$$

where $\{W\} = \{w_0, w_1, w_2, \dots, w_n\}^T$ and $\{F\} = \{f_0, f_1, f_2, \dots, f_n\}^T$ represent the beam settlement vector and the additional load vector, respectively; and $[K]$ is defined as the displacement stiffness matrix of the beam, which can be expressed as

$$[K] = \begin{bmatrix} \frac{30}{7}a_1 + \frac{15}{7}a_2 + a_3 & -\frac{32}{7}a_1 - \frac{2}{7}a_2 & \frac{16}{7}a_1 + \frac{1}{7}a_2 & & & & & & & & \\ & \frac{15}{7}a_1 + a_2 & -\frac{9}{7}a_1 + a_3 & \frac{1}{7}a_1 + a_2 & a_1 & & & & & & \\ & & a_1 & a_2 & a_3 & a_2 & a_1 & & & & \\ & & & a_1 & a_2 & a_3 & a_2 & a_1 & & & \\ & & & & \ddots & \ddots & \ddots & \ddots & \ddots & & \\ & & & & & a_1 & a_2 & a_3 & a_2 & a_1 & \\ & & & & & & a_1 & a_2 & a_3 & & \\ & & & & & & & a_1 & a_2 & & \\ & & & & & & & & a_1 & & \\ & & & & & & & & & \frac{1}{7}a_1 + a_2 & -\frac{9}{7}a_1 + a_3 & \frac{15}{7}a_1 + a_2 \\ & & & & & & & & & \frac{16}{7}a_1 + \frac{1}{7}a_2 & -\frac{32}{7}a_1 - \frac{2}{7}a_2 & \frac{30}{7}a_1 + \frac{15}{7}a_2 + a_3 \end{bmatrix} \quad (27)$$

Similar to Equation (15), Equations (17)–(19) can be further written in the matrix form as the following equations:

$$\{\theta\} = [K_\theta]\{W\} \quad (28)$$

$$\{M\} = [K_M]\{W\} \quad (29)$$

$$\{Q\} = [K_O] \{W\} \quad (30)$$

where $\{\theta\} = \{\theta_0, \theta_1, \theta_2, \dots, \theta_n\}^T$, $\{M\} = \{M_0, M_1, M_2, \dots, M_n\}^T$, and $\{Q\} = \{Q_0, Q_1, Q_2, \dots, Q_n\}^T$ denote the vectors of the rotation angle, bending moment, and shear force of the beam, respectively; $[K_\theta]$, $[K_M]$, and $[K_Q]$ represent the stiffness matrices of the rotation angle, bending moment, and shear force of the beam, respectively, which can be expressed as follows:

$$[K_\theta] = \frac{1}{12l} \begin{bmatrix} -\frac{90}{7} & \frac{96}{7} & -\frac{6}{7} & & & & & & \\ -\frac{41}{7} & -\frac{9}{7} & \frac{57}{7} & -1 & & & & & \\ 1 & -8 & 0 & 8 & -1 & & & & \\ & 1 & -8 & 0 & 8 & -1 & & & \\ & & \ddots & \ddots & \ddots & \ddots & \ddots & & \\ & & & 1 & -8 & 0 & 8 & -1 & \\ & & & & 1 & -8 & 0 & 8 & -1 \\ & & & & & 1 & -\frac{57}{7} & \frac{9}{7} & \frac{41}{7} \\ & & & & & & \frac{6}{7} & -\frac{96}{7} & \frac{90}{7} \end{bmatrix} \quad (31)$$

$$[K_M] = -\frac{EI}{12l^2} \begin{bmatrix} 0 & 0 & 0 & & & & & & & \\ \frac{97}{7} & -\frac{201}{7} & \frac{111}{7} & -1 & & & & & & \\ -1 & 16 & -30 & 16 & -1 & & & & & \\ & -1 & 16 & -30 & 16 & -1 & & & & \\ & & \ddots & \ddots & \ddots & \ddots & \ddots & & & \\ & & & -1 & 16 & -30 & 16 & -1 & & \\ & & & & -1 & 16 & -30 & 16 & -1 & \\ & & & & & -1 & \frac{111}{7} & -\frac{201}{7} & \frac{97}{7} & \\ & & & & & & 0 & 0 & 0 & \end{bmatrix} \quad (32)$$

$$[K_Q] = -\frac{EI}{2l^3} \begin{bmatrix} 0 & 0 & 0 & & & & & & \\ -\frac{1}{7} & \frac{9}{7} & -\frac{15}{7} & 1 & & & & & \\ -1 & 2 & 0 & -2 & 1 & & & & \\ & -1 & 2 & 0 & -2 & 1 & & & \\ & & \ddots & \ddots & \ddots & \ddots & \ddots & & \\ & & & -1 & 2 & 0 & -2 & 1 & \\ & & & & -1 & 2 & 0 & -2 & 1 \\ & & & & & -1 & \frac{15}{7} & -\frac{9}{7} & \frac{1}{7} \\ & & & & & & 0 & 0 & 0 \end{bmatrix} \quad (33)$$

Finally, the beam settlements can be calculated by solving Equation (26). In addition, the corresponding rotation angles, bending moments, and shear forces of the beam can be subsequently determined according to Equations (28)–(30).

3. Verifications

Two typical relative positions between the tunnel and the existing building are utilized to verify the accuracy of the proposed method. As for the building axis perpendicular to the tunnel axis, the building settlement derived from the proposed method are compared with those from the finite element analysis performed by Maleki et al. [17] and the Winkler-based method. Furthermore, the finite difference method is employed to compute the building settlement when the building axis is parallel to the tunnel axis. The results of the finite difference method are also compared with those from the proposed and Winkler-based methods.

3.1. Building Axis Perpendicular to Tunnel Axis

Maleki et al. [17] studied the effects of building characteristics on the tunnel–building interaction using the finite element code PLAXIS 3D. The soil is considered to be elastoplastic material with isotropic hardening mechanism. The elastic modulus, Poisson's ratio, cohesion, and internal friction angle of the soil are 56.7 MPa, 0.2, 0.25 kPa, and 40°, respectively. An 8.85 m diameter tunnel with a depth to tunnel axis of 17.7 m is excavated. A gap parameter of 11.8 mm is used in calculation. The tunnel runs perpendicular to the building axis, while the eccentricity between the tunnel and the existing building is zero ($\alpha = 0$, $y \rightarrow -\infty$, $s_2 = -50.0$ m). The existing building with a varying number of stories is modeled by the equivalent elastic beam, and the parameters of the equivalent beam are shown in Table 1.

Table 1. Parameters of equivalent beam [17].

Building Stories	Equivalent Beam				
	Length L (m)	Weight W (kN/m/m)	Axial Stiffness EA (kN/m)	Bending Stiffness EI (kN·m ² /m)	Poisson's Ratio ν_b
4	100	40	1.725×10^7	3.989×10^8	0.25
8		80	3.105×10^7	2.393×10^9	

The building settlement obtained from the proposed method, finite element method, and Winkler-based method is shown in Figure 6. It can be observed that the shapes of the two predicted building settlement troughs are in accordance with those from the finite element method, and the maximum building settlement acquired from these three methods all occur above the tunnel axis. Compared with the results given by Maleki et al. [17], the proposed method and the Winkler-based method slightly underestimate the building settlement for the 4-story building, whereas the comparison results are opposite in respect of the 8-story building. With the increase in the transverse distance from the tunnel axis, the differences between the two predicted building settlements and the results of the finite element method gradually decrease to 0 for the 4-story building. In general, the proposed

method offers satisfactory building settlement subjected to tunnel excavation. It is worth noting that the proposed method yields building settlements close to those provided by the Winkler-based method, which is consistent with the analysis of Liang et al. [45].

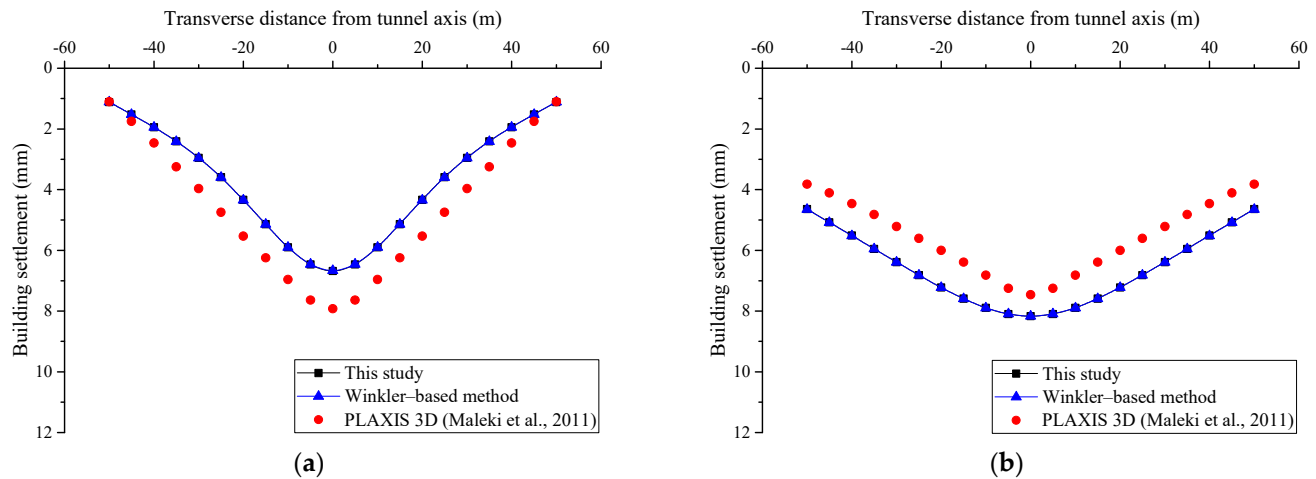


Figure 6. Comparison with building settlement from finite element method: (a) 4 stories; (b) 8 stories [17].

3.2. Building Axis Parallel to Tunnel Axis

As shown in Figure 2, with regard to the building axis parallel to and directly above the tunnel axis ($\alpha = 90^\circ$, $s_2 = 0$), the three-dimensional finite difference analysis using FLAC 3D is conducted to reproduce the building settlements caused by tunneling process. The diameter of the circular tunnel is 6.0 m based on the area equivalent method, and the depth to tunnel axis is 15.0 m (Figure 7). The dimensions of the numerical model are 60.0 m in width, 36.0 m in height, and 80.0 m in length, which are sufficiently large to eliminate the boundary effect. The normal displacements of the four vertical boundaries are fixed while the nodes at the bottom boundary are fixed in both vertical and horizontal directions, and the top boundary of the numerical model is left free. The soil is modeled as a linear elastic–perfectly plastic material with the Mohr–Coulomb failure criterion. The isotropic elastic model is employed for simulations of the 0.3 m thick tunnel lining and the existing building. The existing building is ideally represented by an equivalent beam with length 20.0 m, width 2.0 m, and height 1.0 m. The physical and mechanical parameters of the numerical model are shown in Table 2.

The numerical simulation consists of the following stages [19]: (1) initialization of the geostatic stress in the ground under greenfield condition; (2) resetting the ground movements to zero, followed by the activation of the equivalent beam; and (3) tunnel excavation and lining installation. The tunneling process is simulated one step advance at a time as a repeated sequence of: (1) removing the unit soil at the excavation step (1.0 m); (2) releasing the soil stress; (3) generating the lining elements at the excavation step.

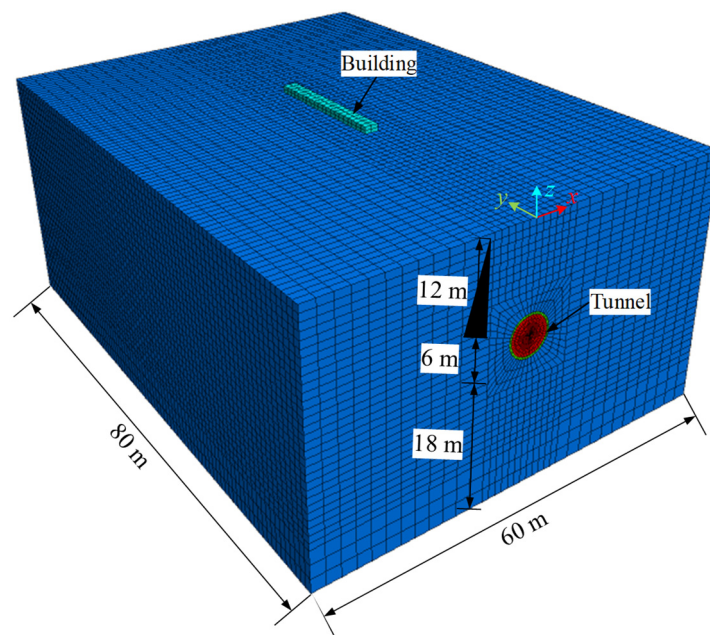


Figure 7. Finite difference model.

Table 2. Physical and mechanical parameters of numerical model.

Material	Unit Weight γ (kN/m ³)	Elastic Modulus E (MPa)	Poisson's Ratio ν	Cohesion c (kPa)	Internal Friction Angle φ (°)
Soil	20	30	0.3	10	30
Lining	25	3.0×10^4	0.2	–	–
Building	25	3.0×10^4	0.2	–	–

Figure 8 shows the building settlements above the tunnel axis calculated by FLAC 3D compared with those from the proposed method and Winkler-based method ($g = 30.0$ mm, $d = 0$). The trends of the building settlement curves estimated by the two analytical methods are similar to the finite difference results in three cases. The maximum and minimum building settlements calculated through these three methods are all located at the left and right ends of the building, respectively. The magnitudes of the building settlements gained from the proposed method agree better with the finite difference results than those from the Winkler-based method, especially in the case of $s_1 = -20.0$ m. The results of the Winkler-based method are slightly smaller than those from the proposed method, which implies that the building settlements are not substantially subjected to the shear stiffness of the subgrade. Overall, the proposed method can be adopted to effectively and rapidly predict the building response resulting from shallow tunneling.

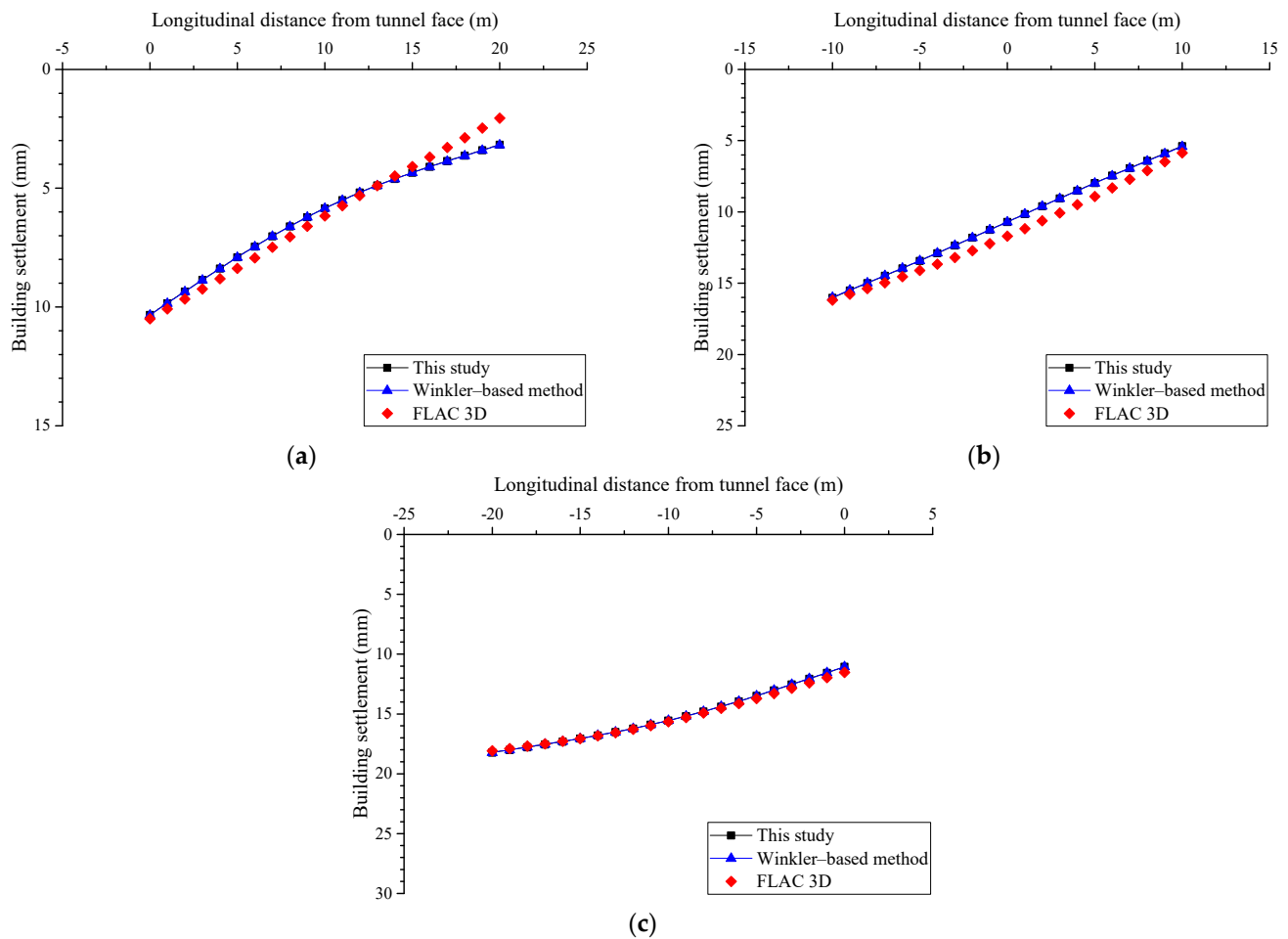


Figure 8. Comparison with building settlement from finite difference method: (a) $s_1 = 0$; (b) $s_1 = -10.0$ m; (c) $s_1 = -20.0$ m.

4. Parametric Analysis

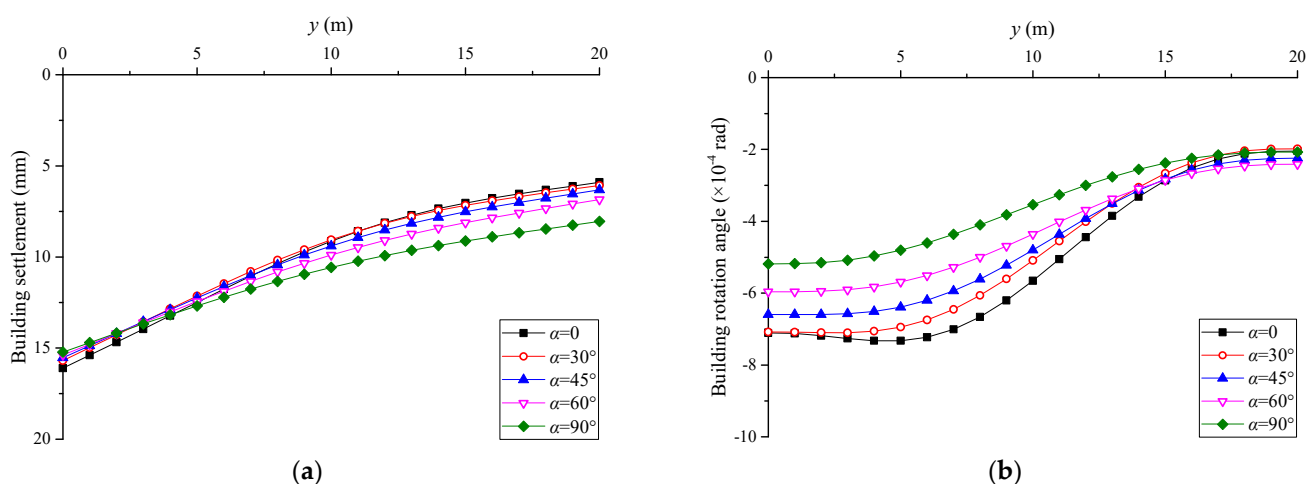
To further understand the building response associated with tunnel excavation, the effects of different factors on the settlements, rotation angles, bending moments, and shear forces of a masonry building are investigated, including the alignment angle, distance from tunnel face, elastic modulus and Poisson's ratio of the soil, bending stiffness, and gap parameter. The values of these six factors are listed in Table 3. For direct comparisons with the corresponding different factors, a basic case is selected and the absolute values of the results are used in this section. The parameters of the soil and tunnel are the same as those in Section 3.2. The building axis is parallel to and directly above the tunnel axis and $s_1 = -20.0$ m (Figure 2). The length, equivalent bending stiffness, and equivalent vertical uniform pressure of the existing building are set to 20.0 m, $1500 \text{ MN}\cdot\text{m}^2$, and 100 kPa, respectively [39].

Table 3. Parameters used for analysis.

Number	Alignment Angle α (°)	Distance from Tunnel Face s_1 (m)	Soil Elastic Modulus E_s (MPa)	Poisson's Ratio ν	Bending Stiffness EI (MN·m ²)	Gap Parameter g (mm)
1	0, 30, 45, 60, 90	0	30	0.3	1500	30
2	90	20, 0, −5, −10, −15 −20, −40	30	0.3	1500	30
3	90	−20	20, 30, 40, 50, 60	0.3	1500	30
4	90	−20	30	0.1, 0.2, 0.3, 0.4, 0.5	1500	30
5	90	−20	30	0.3	500, 1000, 1500, 2000, 2500	30
6	90	−20	30	0.3	1500	10, 20, 30, 40, 50

4.1. Alignment Angle

The effects of the alignment angle on the building response in the case of $s_1 = s_2 = 0$ are shown in Figure 9. As the alignment angle increases from 0° to 90°, the maximum building settlement at the left end of the building decreases from 16.1 to 15.2 mm, while the minimum building settlement at the right end of the building increases from 5.9 to 8.0 mm (Figure 9a). For each alignment angle, the building settlements gradually decrease along the building axis. The rotation angles generally decrease with an increase in the alignment angle. The position where the maximum rotation angle occurs moves from $y = 5.0$ m to $y = 0$, and the rotation angle at $y = 20.0$ m is the minimum (Figure 9b). Along the building axis, the rotation angles first increase and then decrease when $\alpha = 0$, and gradually decrease in the other four cases. The increase in the alignment angle leads to the decreases in the maximum bending moments (including the maximum positive and negative bending moments), and causes the position of the maximum negative moment to move toward the tunnel face, as shown in Figure 9c. Similar characteristics can also be observed in Figure 9d, and the position of the maximum positive shear force is fixed at $y = 16.0$ m. On the condition $\alpha = 90^\circ$, the bending moments are all nonpositive and approximately symmetric with respect to the building centerline ($y = 10.0$ m). Meanwhile, the shear forces are approximately antisymmetric with respect to the building centerline.

**Figure 9.** Cont.

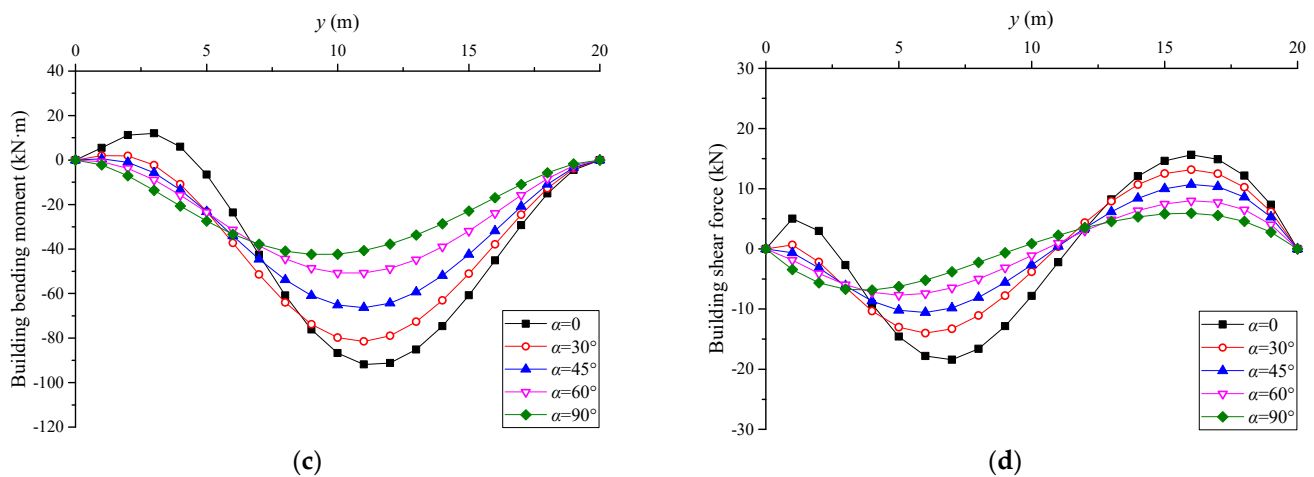


Figure 9. Building response with different alignment angles: (a) settlement; (b) rotation angle; (c) bending moment; (d) shear force.

4.2. Distance from Tunnel Face

Figure 10 shows the variations in the building response with different distances from the tunnel face. The remarkable increases in the building settlement with the advancing tunnel can be seen in Figure 10a, while the differential settlement of the building first increases and then decreases. The uniform building settlements are produced when the tunnel face is far away from the building ($s_1 = 20.0$ m and $s_1 = -40.0$ m). The settlement difference between the two ends of the building reaches the maximum when the tunnel face is located at the middle of the building ($s_1 = -10.0$ m), coinciding with the results described in Section 3.2. As shown in Figure 10b, by decreasing the distance from the tunnel face from 20.0 to -5.0 m, the rotation angles gradually increase along the direction of the tunnel. The trends are opposite as the distance from the tunnel face decreases from -15.0 to -40.0 m. In particular, the rotation angles are symmetric with respect to the building centerline where the maximum rotation angle appears, assuming that $s_1 = -10.0$ m.

The maximum bending moments first increase and then decrease with the decrease in the distance from the tunnel face (Figure 10c). Both the maximum positive and negative bending moments appear at $y = 10.0$ m, corresponding to $s_1 = -20.0$ m and $s_1 = 0$, respectively. For $s_1 = 0$ and $s_1 = -20.0$ m, the maximum negative shear forces appear at $y = 4.0$ and $y = 16.0$ m, respectively. For $s_1 = -5.0$ m and $s_1 = -15.0$ m, the maximum positive shear forces appear at $y = 17.0$ m and $y = 3.0$ m, respectively (Figure 10d). In the case of $s_1 = -10.0$ m, the bending moments and the shear forces are antisymmetric and symmetric with respect to the building centerline, respectively. Moreover, when the tunnel face is located outside the two ends of the building ($s_1 = 20.0, 0, -20.0, -40.0$ m), the shear forces at the middle of the building are about zero.

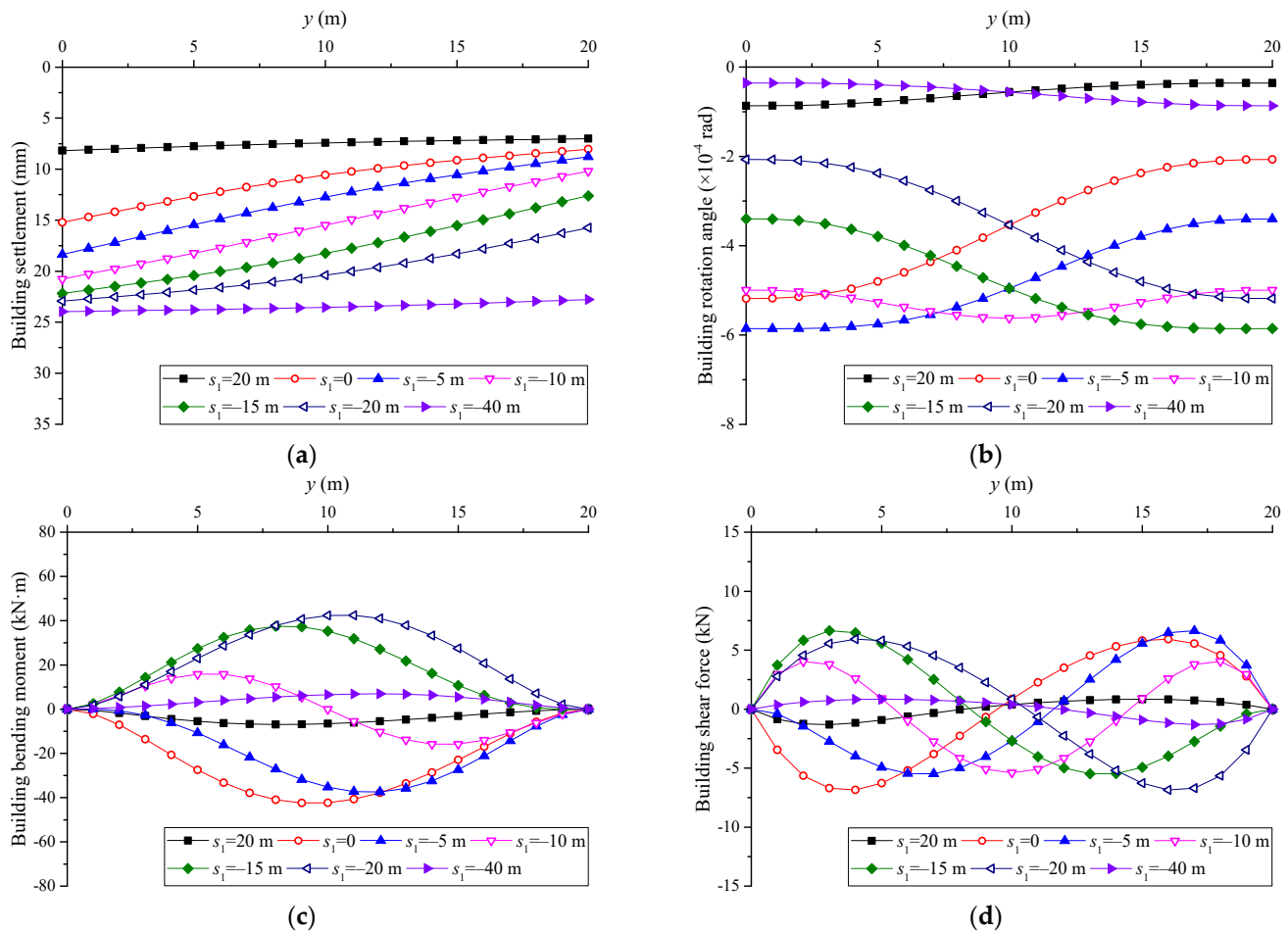


Figure 10. Building response with different distances from tunnel face: (a) settlement; (b) rotation angle; (c) bending moment; (d) shear force.

4.3. Soil Elastic Modulus

The effects of the soil elastic modulus on the building response are shown in Figure 11. The increase in the soil elastic modulus can obviously decrease the building settlement (Figure 11a), which is because the stiffer soil can provide larger resistance to resist the building settlement due to the stress relief. The magnitude of the decrease in the building settlement decreases as the soil elastic modulus increases. With the increase in the soil elastic modulus, the rotation angles gradually decrease in the range $y \leq 10.0$ m and increase in the range $y > 10.0$ m (Figure 11b). The maximum and minimum rotation angles occur at $y = 20.0$ m and $y = 0$, respectively. The bending moments greatly increase and become less sensitive to the soil elastic modulus as the soil elastic modulus increases (Figure 11c). The maximum positive bending moment occurs at the middle of the building, regardless of the variation in the soil elastic modulus. When the soil elastic modulus increases from 20.0 to 60.0 MPa, the maximum positive shear force occurring at $y = 4.0$ m and the maximum negative shear force increase accordingly (Figure 11d). Additionally, the position of the maximum negative shear force moves from $y = 16.0$ m to $y = 17.0$ m.

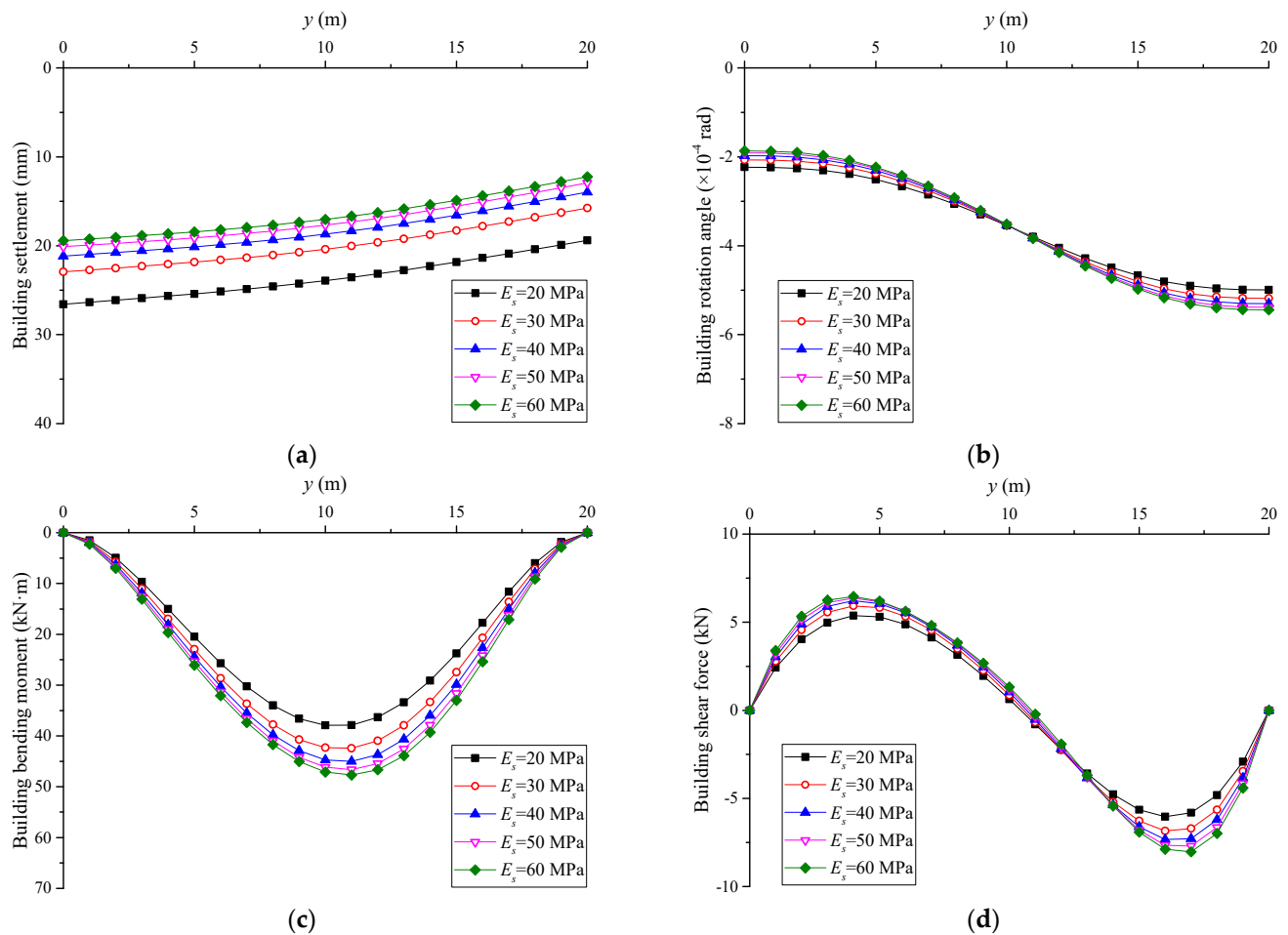


Figure 11. Building response with different soil elastic moduli: (a) settlement; (b) rotation angle; (c) bending moment; (d) shear force.

4.4. Soil Poisson's Ratio

Figure 12 shows the relationships between the soil Poisson's ratio and the building response. Figure 12a shows that the decreases in the settlement and the differential settlement of the building are increasingly significant with a larger soil Poisson's ratio. A notable trend of decreasing rotation angle is observed by the increase in the soil Poisson's ratio (Figure 12b). The maximum and minimum rotation angles occur at the right and left ends of the building, respectively. The bending moments depend highly on and share progressively decreasing trend with the soil Poisson's ratio, as shown in Figure 12c. The effect of the soil Poisson's ratio on the bending moment is mainly reflected around the middle of the building, and is almost negligible near the two ends of the building. The maximum shear forces (including the maximum positive and negative shear forces) gradually decrease as the soil Poisson's ratio increases (Figure 12d). The positions of the maximum positive and negative shear forces are fixed at $y = 4.0$ m and $y = 16.0$ m, respectively, which are independent of the soil Poisson's ratio.

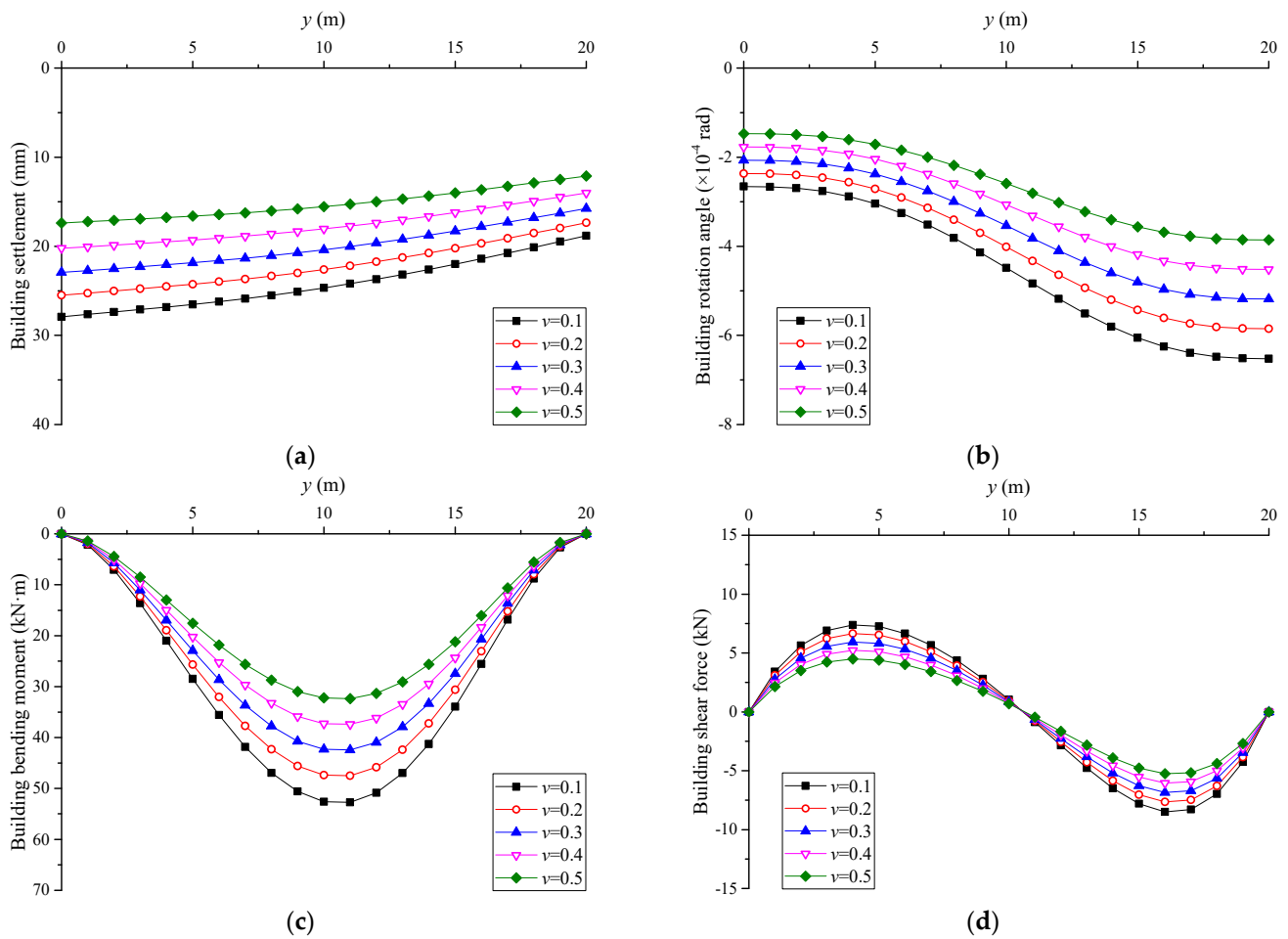


Figure 12. Building response with different soil Poisson's ratios: (a) settlement; (b) rotation angle; (c) bending moment; (d) shear force.

4.5. Bending Stiffness

The effects of the bending stiffness on the building response are shown in Figure 13. The building settlement slightly increases with the increase in the bending stiffness (Figure 13a), indicating that the bending stiffness has little effect on the building settlement. Given by the larger bending stiffness, the rotation angles of the left half of the building gradually increase while those of the right half of the building gradually decrease (Figure 13b). The increase in the bending stiffness results in sharply increased bending moments (Figure 13c), which demonstrates that a stiffer building suffers much larger bending moments than those of a relatively flexible building. The magnitude of the increase in the bending moments decreases when the bending stiffness increases. The maximum shear forces also increase as the bending stiffness increases from 500 to 2500 $\text{MN}\cdot\text{m}^2$ (Figure 13d). Additionally, the y -coordinates of the maximum positive and negative shear forces are fixed at 4.0 m and decrease from 17.0 to 16.0 m, respectively.

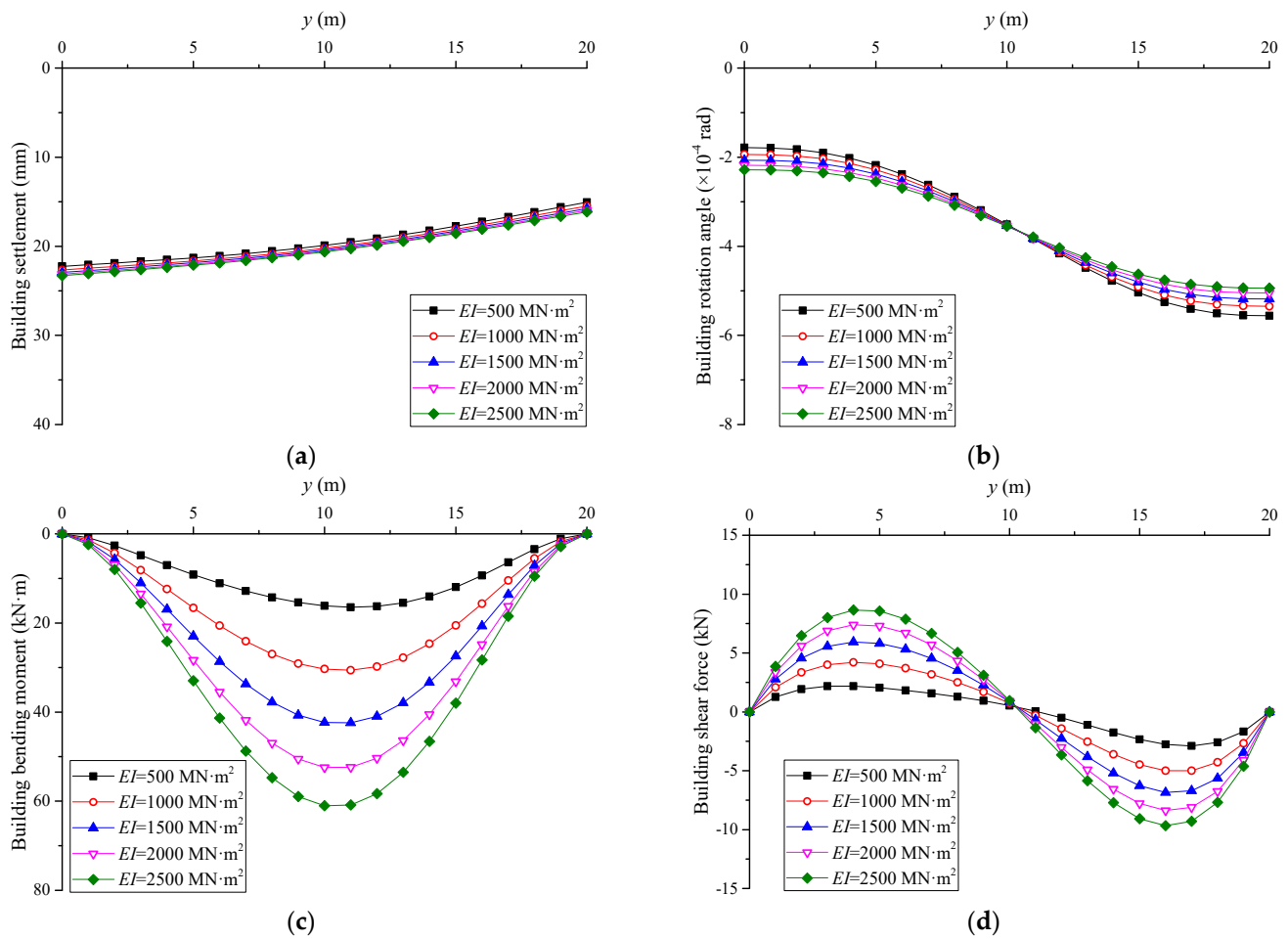


Figure 13. Building response with different bending stiffness: (a) settlement; (b) rotation angle; (c) bending moment; (d) shear force.

4.6. Gap Parameter

Figure 14 shows the settlements, rotation angles, bending moments and shear forces of the existing building under different gap parameters. Contrary to the effect of the soil Poisson's ratio on the building response, the increase in the gap parameter greatly increases the settlement and the differential settlement of the building (Figure 14a). Figure 14b indicates that the larger the gap parameter is, the larger the rotation angles are. As the gap parameter increases from 10.0 to 50.0 mm, the absolute value of the maximum rotation angle increases from 1.7×10^{-4} to 8.7×10^{-4} rad, while that of the minimum rotation angle increases from 0.7×10^{-4} to 3.5×10^{-4} rad. It can be found that the bending moments achieve rapid increase when the gap parameter becomes larger, and the magnitude of the increase in the bending moments increases as the gap parameter increases (Figure 14c). With an increase in the gap parameter, the maximum positive and negative shear forces gradually increase according to Figure 14d, and always appear at $y = 4.0$ m and $y = 16.0$ m, respectively.

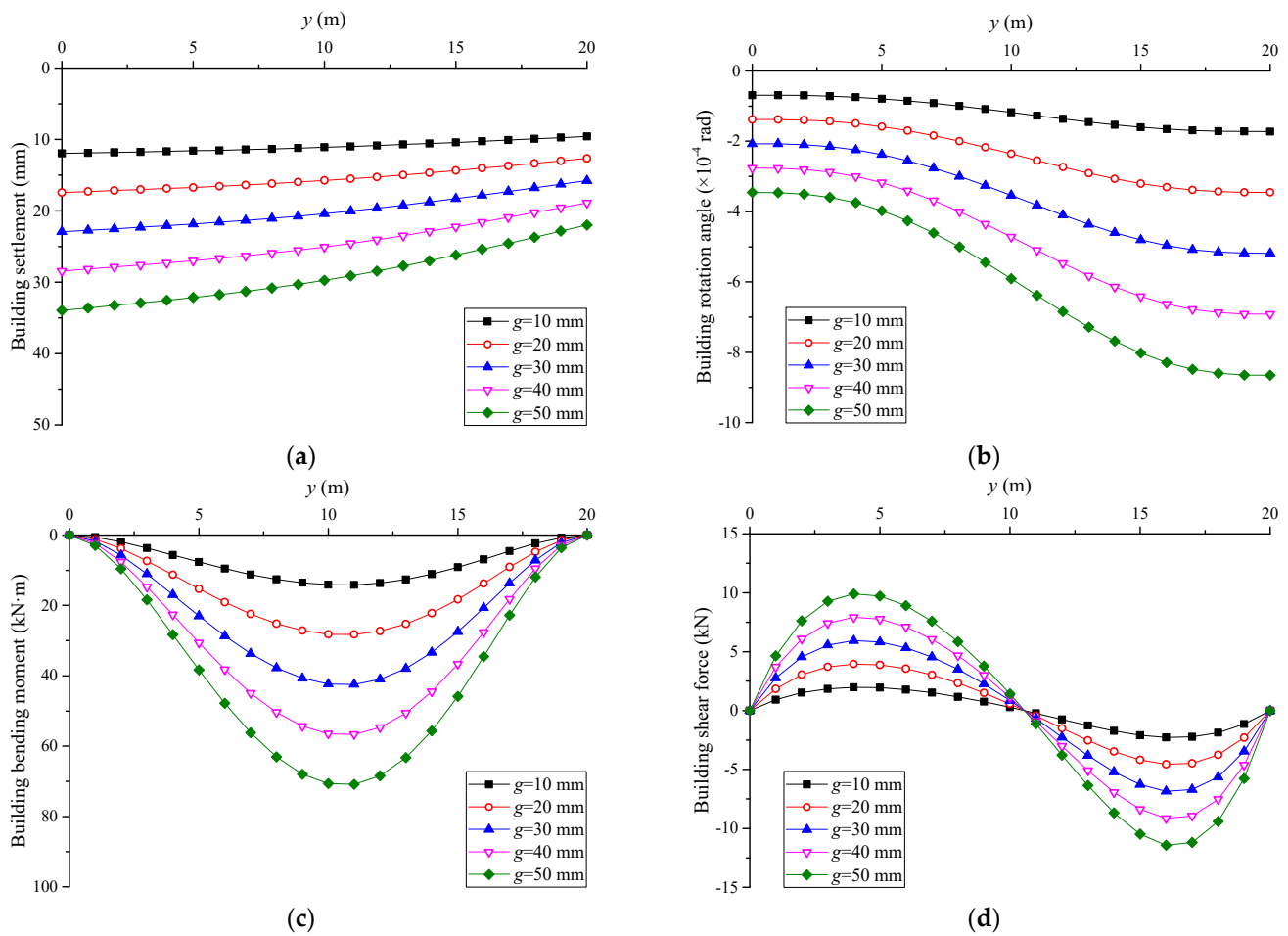


Figure 14. Building response with different gap parameters: (a) settlement; (b) rotation angle; (c) bending moment; (d) shear force.

5. Conclusions

An analytical method for predicting the strip foundation building response induced by three-dimensional ground settlement due to shallow tunneling is presented in this paper. The tunneling process and different alignment angles are taken into account in the proposed method. The effects of six typical factors on the building response are illustrated. The main conclusions follow:

- (1) The reliability of the proposed method is determined in comparison with finite element and finite difference analysis. The results obtained from the proposed method show good agreement with the two numerical results and close to those from the Winkler-based method.
- (2) The building settlement increases with the increase in the bending stiffness and gap parameter, and decrease as the distance from the tunnel face increases, and the elastic modulus and Poisson's ratio of the soil increase. The differential settlement of the building increases as the alignment angle decreases and the gap parameter increases, and reaches a maximum when the tunnel face is located at the middle of the building.
- (3) Increases in the alignment angle and soil Poisson's ratio, and the decrease in the gap parameter can decrease the rotation angles. By increasing the soil elastic modulus, the rotation angles of the left half of the building decrease while those of the right half of the building increase. The opposite trend can be observed for the bending stiffness. When the tunnel face arrives at the middle of the building, the rotation angles are symmetric with respect to the building centerline.

- (4) The maximum bending moments and the maximum shear forces gradually decrease with a larger alignment angle. The bending moments and the maximum shear forces increase as the soil elastic modulus, bending stiffness, and gap parameter increase, and decrease with the increase in the soil Poisson's ratio. The maximum bending moments occur at the middle of the building, and the maximum shear forces appear at about one-fifth and four-fifths of the building length when the tunnel face is located at the two ends of the building.
- (5) The influence of the plastic behavior of the soil and the contact state between the building foundation and the underlying soil on the building response need to be considered in a further study.

Author Contributions: Conceptualization, L.Y. and Y.L.; methodology, L.Y. and G.W.; software, Y.L. and L.C.; formal analysis, L.C.; investigation, L.Y. and G.W.; data curation, G.W. and Y.L.; writing—original draft preparation, L.Y.; writing—review and editing, Q.F.; supervision, D.Z. All authors have read and agreed to the published version of the manuscript.

Funding: This research was funded by the Research Project of Beijing Mass Transit Railway Operation Corp. Ltd., grant number 2021000581000007, and the National Natural Science Foundation of China, grant numbers 52108376 and 51738002.

Institutional Review Board Statement: Not applicable.

Informed Consent Statement: Not applicable.

Data Availability Statement: Data are contained within this article.

Acknowledgments: The authors thank the reviewers for their great help on the article during the review process.

Conflicts of Interest: The authors declare no conflict of interest. The funders had no role in the design of the study; in the collection, analyses, or interpretation of data; in the writing of the manuscript, or in the decision to publish the results.

References

1. Yu, L.; Zhang, D.L.; Fang, Q.; Cao, L.Q.; Xu, T.; Li, Q.Q. Surface settlement of subway station construction using pile-beam-arch approach. *Tunn. Undergr. Sp. Tech.* **2019**, *90*, 340–356. [\[CrossRef\]](#)
2. Wu, H.N.; Shen, S.L.; Chen, R.P.; Zhou, A. Three-dimensional numerical modelling on localised leakage in segmental lining of shield tunnels. *Comput. Geotech.* **2020**, *122*, 103549. [\[CrossRef\]](#)
3. Zhang, N.; Zhang, N.; Zheng, Q.; Xu, Y.S. Real-time prediction of shield moving trajectory during tunnelling using GRU deep neural network. *Acta. Geotech.* **2021**, *17*, 1167–1182. [\[CrossRef\]](#)
4. Fang, Q.; Zhang, D.L.; Wong, L.N.Y. Shallow tunnelling method (STM) for subway station construction in soft ground. *Tunn. Undergr. Sp. Tech.* **2012**, *29*, 10–30. [\[CrossRef\]](#)
5. Li, P.F.; Wei, Y.J.; Zhang, M.J.; Huang, Q.F.; Wang, F. Influence of non-associated flow rule on passive face instability for shallow shield tunnels. *Tunn. Undergr. Sp. Tech.* **2022**, *119*, 104202. [\[CrossRef\]](#)
6. Yu, L.; Zhang, D.L.; Fang, Q.; Cao, L.Q.; Zhang, Y.; Xu, T. Face stability of shallow tunnelling in sandy soil considering unsupported length. *Tunn. Undergr. Sp. Tech.* **2020**, *102*, 103445. [\[CrossRef\]](#)
7. Basmaji, B.; Deck, O.; Al Heib, M. Analytical model to predict building deflections induced by ground movements. *Eur. J. Environ. Civ. Eng.* **2017**, *10*, 1–23. [\[CrossRef\]](#)
8. Elkayam, I.; Klar, A. Nonlinear elastoplastic formulation for tunneling effects on superstructures. *Can. Geotech. J.* **2019**, *56*, 956–969. [\[CrossRef\]](#)
9. Franza, A.; DeJong, M.J. Elastoplastic solutions to predict tunneling-induced load redistribution and deformation of surface structures. *J. Geotech. Geoenviron. Eng.* **2019**, *145*, 4019007. [\[CrossRef\]](#)
10. El Kahi, E.; Deck, O.; Khouri, M.; Mehdizadeh, R.; Rahme, P. A new simplified meta-model to evaluate the transmission of ground movements to structures integrating the elastoplastic soil behavior. *Structures* **2020**, *23*, 324–334. [\[CrossRef\]](#)
11. Franza, A.; Acikgoz, S.; DeJong, M.J. Timoshenko beam models for the coupled analysis of building response to tunneling. *Tunn. Undergr. Sp. Tech.* **2020**, *96*, 103160. [\[CrossRef\]](#)
12. Mair, R.J.; Taylor, R.N.; Burland, J.B. Prediction of ground movements and assessment of risk of building damage due to bored tunnelling. In Proceedings of the International Symposium on Geotechnical Aspects of Underground Construction in Soft Ground, London, UK, 15–17 April 1996; pp. 713–718.
13. Camos, C.; Molins, C. 3D analytical prediction of building damage due to ground subsidence produced by tunneling. *Tunn. Undergr. Sp. Tech.* **2015**, *50*, 424–437. [\[CrossRef\]](#)

14. Franco, V.H.; Gitirana, G.D.N.; de Assis, A.P. Probabilistic assessment of tunneling-induced building damage. *Comput. Geotech.* **2019**, *113*, 103097. [[CrossRef](#)]
15. Son, M.; Cording, E.J. Estimation of building damage in a 3D distorting structure to tunnel and underground excavation-induced ground movements. *Tunn. Undergr. Sp. Tech.* **2020**, *97*, 103222. [[CrossRef](#)]
16. Franzius, J.N.; Potts, D.M.; Burland, J.B. The response of surface structures to tunnel construction. *Proc. ICE-Geotech. Eng.* **2006**, *159*, 3–17. [[CrossRef](#)]
17. Maleki, M.; Sereshteh, H.; Mousivand, M.; Bayat, M. An equivalent beam model for the analysis of tunnel-building interaction. *Tunn. Undergr. Sp. Tech.* **2011**, *26*, 524–533. [[CrossRef](#)]
18. Giardina, G.; Van de Graaf, A.V.; Hendriks, M.A.N.; Rots, J.G.; Marini, A. Numerical analysis of a masonry facade subject to tunnelling-induced settlements. *Eng. Struct.* **2013**, *54*, 234–247. [[CrossRef](#)]
19. Fagnoli, V.; Gragnano, C.G.; Boldini, D.; Amorosi, A. 3D numerical modelling of soil-structure interaction during EPB tunnelling. *Geotechnique* **2015**, *65*, 23–37. [[CrossRef](#)]
20. Boldini, D.; Losacco, N.; Bertolin, S.; Amorosi, A. Finite element modelling of tunnelling-induced displacements on framed structures. *Tunn. Undergr. Sp. Tech.* **2018**, *80*, 222–231. [[CrossRef](#)]
21. Jenck, O.; Dias, D. 3D-finite difference analysis of the interaction between concrete building and shallow tunneling. *Geotechnique* **2004**, *54*, 519–528. [[CrossRef](#)]
22. Son, M. Response analysis of nearby structures to tunneling-induced ground movements in clay soils. *Tunn. Undergr. Sp. Tech.* **2016**, *56*, 90–104. [[CrossRef](#)]
23. Farrell, R.; Mair, R.; Sciotti, A.; Pigorini, A. Building response to tunnelling. *Soils Found.* **2014**, *54*, 269–279. [[CrossRef](#)]
24. Ritter, S.; Giardina, G.; Dejong, M.J.; Mair, R.J. Influence of building characteristics on tunnelling-induced ground movements. *Geotechnique* **2017**, *67*, 926–937. [[CrossRef](#)]
25. Ritter, S.; Giardina, G.; Franza, A.; DeJong, M.J. Building deformation caused by tunneling: Centrifuge modeling. *J. Geotech. Geoenviron. Eng.* **2020**, *146*, 4020017. [[CrossRef](#)]
26. Shahin, H.M.; Nakai, T.; Hinokio, M.; Kurimoto, T.; Sada, T. Influence of surface loads and construction sequence on ground response due to tunneling. *Soils Found.* **2004**, *44*, 71–84. [[CrossRef](#)]
27. Son, M.; Cording, E.J. Estimation of building damage due to excavation-induced ground movements. *J. Geotech. Geoenviron. Eng.* **2005**, *131*, 162–177.
28. Giardina, G.; Marini, A.; Hendriks, M.A.N.; Rots, J.G.; Rizzardini, F.; Giuriani, E. Experimental analysis of a masonry facade subject to tunnelling-induced settlement. *Eng. Struct.* **2012**, *45*, 421–434. [[CrossRef](#)]
29. Frischmann, W.W.; Hellings, J.E.; Gittos, G.; Snowden, C. Protection of the Mansion House against damage caused by ground movements due to the Docklands Light Railway extension. *Proc. ICE-Geotech. Eng.* **1994**, *107*, 65–76. [[CrossRef](#)]
30. Dimmock, P.S.; Mair, R.J. Effect of building stiffness on tunnelling-induced ground movement. *Tunn. Undergr. Sp. Tech.* **2008**, *23*, 438–450. [[CrossRef](#)]
31. Zhang, D.L.; Fang, Q.; Hou, Y.J.; Li, P.F.; Wong, L.N.Y. Protection of buildings against damages as a result of adjacent large-span tunneling in shallowly buried soft ground. *J. Geotech. Geoenviron. Eng.* **2013**, *139*, 903–913. [[CrossRef](#)]
32. Fu, J.Y.; Yang, J.S.; Zhang, X.M.; Klapperich, H.; Abbas, S.M. Response of the ground and adjacent buildings due to tunnelling in completely weathered granitic soil. *Tunn. Undergr. Sp. Tech.* **2014**, *43*, 377–388. [[CrossRef](#)]
33. Bloodworth, A.G.; Houlsby, G.T. Analysis of pre-vault tunnelling interaction with buildings. *Proc. ICE-Geotech. Eng.* **2017**, *170*, 99–116. [[CrossRef](#)]
34. Pasternak, P.L. *On a New Method of Analysis of an Elastic Foundation by Means of Two Foundation Constants*; Gosudarstvennoe Izdatelstvo Literatury po Stroitelstvu i Arkhitekture: Moscow, Russia, 1954.
35. Yu, L. Study on Mechanisms and Chain Effect of Disasters Due to Subway Tunnel Excavation. Ph.D. Thesis, Beijing Jiaotong University, Beijing, China, 2021. (In Chinese).
36. Loganathan, N.; Poulos, H.G. Analytical prediction for tunneling-induced ground movements in clays. *J. Geotech. Geoenviron. Eng.* **1998**, *124*, 846–856. [[CrossRef](#)]
37. Lee, K.M.; Rowe, R.K.; Lo, K.Y. Subsidence owing to tunneling. I. Estimating the gap parameter. *Can. Geotech. J.* **1992**, *29*, 929–940. [[CrossRef](#)]
38. Maynar, M.M.; Rodriguez, L.M. Predicted versus measured soil movements induced by shield tunnelling in the Madrid Metro extension. *Can. Geotech. J.* **2005**, *42*, 1160–1172. [[CrossRef](#)]
39. Ding, Z. Prediction of Deformation and Study on the Influence of Shield Tunnel on Adjacent Buildings. Ph.D. Thesis, Zhejiang University, Hangzhou, China, 2014. (In Chinese).
40. Vesic, A.B. Bending of beams resting on isotropic elastic solid. *J. Eng. Mech. Div.* **1961**, *87*, 35–53. [[CrossRef](#)]
41. Tanahashi, H. Formulas for an infinitely long Bernoulli-Euler beam on the Pasternak model. *Soils Found.* **2004**, *44*, 109–118. [[CrossRef](#)]
42. Xu, L. Study on the Longitudinal Settlement of Shield Tunnel in Soft Soil. Ph.D. Thesis, Tongji University, Shanghai, China, 2005. (In Chinese).
43. Zhang, Z.G.; Huang, M.S.; Xu, C.; Jiang, Y.J.; Wang, W.D. Simplified solution for tunnel-soil-pile interaction in Pasternak's foundation model. *Tunn. Undergr. Sp. Tech.* **2018**, *78*, 146–158. [[CrossRef](#)]

-
44. Xia, J.W.; Yuan, Y.S.; Dong, Z.Z. Mechanism study on subsoil-strap footing-framework interaction in mining subsidence area. *Chinese J. Geotech. Eng.* **2007**, *29*, 537–541. (In Chinese)
 45. Liang, R.Z.; Xia, T.D.; Huang, M.S.; Lin, C.G. Simplified analytical method for evaluating the effects of adjacent excavation on shield tunnel considering the shearing effect. *Comput. Geotech.* **2017**, *81*, 167–187. [[CrossRef](#)]